

# Spin gap in a quasi-one-dimensional $S = \frac{1}{2}$ antiferromagnet: $\text{Cu}_2(1,4\text{-Diazacycloheptane})_2\text{Cl}_4$

Philip R. Hammar, Daniel H. Reich, and Collin Broholm

*Department of Physics and Astronomy, The Johns Hopkins University, Baltimore, MD 21218*

Frans Trouw

*IPNS, Argonne National Laboratories, Argonne, IL 60439*

(October 21, 2018)

$\text{Cu}_2(1,4\text{-diazacycloheptane})_2\text{Cl}_4$  contains double chains of spin- $\frac{1}{2}$   $\text{Cu}^{2+}$  ions. We report ac susceptibility, specific heat, and inelastic neutron scattering measurements on this material. The magnetic susceptibility,  $\chi(T)$ , shows a rounded maximum at  $T = 8$  K indicative of a low dimensional antiferromagnet with no zero field magnetic phase transition. We compare the  $\chi(T)$  data to exact diagonalization results for various one dimensional spin Hamiltonians and find excellent agreement for a spin ladder with intra-rung coupling  $J_1 = 1.143(3)$  meV and two mutually frustrating inter-rung interactions:  $J_2 = 0.21(3)$  meV and  $J_3 = 0.09(5)$  meV. The specific heat in zero field is exponentially activated with an activation energy  $\Delta = 0.89(1)$  meV. A spin gap is also found through inelastic neutron scattering on powder samples which identify a band of magnetic excitations for  $0.8 < \hbar\omega < 1.5$  meV. Using sum-rules we derive an expression for the dynamic spin correlation function associated with non-interacting propagating triplets in a spin ladder. The van-Hove singularities of such a model are not observed in our scattering data indicating that magnetic excitations in  $\text{Cu}_2(1,4\text{-diazacycloheptane})_2\text{Cl}_4$  are more complicated. For magnetic fields above  $H_{c1} \simeq 7.2$  T specific heat data versus temperature show anomalies indicating a phase transition to an ordered state below  $T = 1$  K.

75.50.Ee, 75.40.-s

## I. INTRODUCTION

As a consequence of its quantum criticality, the low-temperature properties of the Heisenberg spin-1/2 antiferromagnetic chain change dramatically with small perturbations. For example, weak coupling between a macroscopic set of spin chains leads to Néel order at  $T = 0$  while modifications to the one dimensional network of spin interactions can induce spin-gaps and suppress Néel order. The gapped phases of one-dimensional spin-1/2 systems are simple examples of a qualitatively new type of magnetism where the many-body eigenstates are more conveniently described in terms of the singlets and triplets of near-neighbor coupled spin pairs, rather than in terms of the Zeeman states of individual spins.

Theorists have established that spin gaps can be induced by bond alternation, [1,2] by frustration due to next-nearest neighbor interactions, [3–5] and by coupling even numbers of chains to form spin ladders. [6,7] Spin-gaps have been observed in the quasi-one-dimensional spin-1/2 systems  $\text{Cu}(\text{NO}_3)_2 \cdot 2.5\text{H}_2\text{O}$  [2,8],  $\text{CuGeO}_3$  [9,10],  $\text{SrCu}_2\text{O}_3$  [11],  $(\text{La}, \text{Sr}, \text{Ca})_{14}\text{Cu}_{24}\text{O}_{41}$ , [12]  $\text{Cu}_2(1,4\text{-Diazacycloheptane})_2\text{Cl}_4$  ( $\text{CuHpCl}$ ) [13–16], and  $(\text{VO})_2\text{P}_2\text{O}_7$  [17–20]. Apart from the spin-Peierls system  $\text{CuGeO}_3$ , all of these other materials were originally thought to be spin ladders. However, subsequent experiments established that  $\text{Cu}(\text{NO}_3)_2 \cdot 2.5\text{H}_2\text{O}$  and  $(\text{VO})_2\text{P}_2\text{O}_7$  actually consist of alternating spin-chains which are perpendicular to the putative spin-ladder. [19,20] This highlights the difficulty of distinguishing between different Hamiltonians with spin gaps on the basis of measurements which mainly probe the magnetic density of states.

This paper is an experimental study of the gapped spin-1/2 system  $\text{CuHpCl}$ . Because magnetic exchange interactions in this material are quite small it is an excellent system in which to study the field and temperature dependence of spin correlations in a gapped spin-1/2 system. [21] The Cu dimer formula units in  $\text{CuHpCl}$  stack to form double chains. Correspondingly the magnetic interactions between Cu spins are thought to yield a spin ladder as shown in Fig. 1 with a spin-Hamiltonian of the form

$$\mathcal{H} = J_1 \sum_i \mathbf{S}_{2i} \cdot \mathbf{S}_{2i+1} + J_2 \sum_i (\mathbf{S}_{2i} \cdot \mathbf{S}_{2i+2} + \mathbf{S}_{2i-1} \cdot \mathbf{S}_{2i+1}) + J_3 \sum_i \mathbf{S}_{2i-1} \cdot \mathbf{S}_{2i}. \quad (1)$$

We report susceptibility, specific heat and neutron scattering experiments which determine the spin gap and magnetic density of states in  $\text{CuHpCl}$ . While our susceptibility and specific heat data can be interpreted in terms of a spin

ladder, details of the inelastic magnetic neutron scattering data are inconsistent with a simple approximation to the dynamic spin correlation function for a spin ladder.

## II. EXPERIMENTAL TECHNIQUES

CuHpCl is monoclinic, with space group  $P2_1/c$  and lattice constants  $a = 13.406(3)$  Å,  $b = 11.454(2)$  Å,  $c = 12.605(3)$  Å and  $\beta = 115.01(2)$ °. [13] The CuHpCl molecules stack to form chains in the (101) direction. The intradimer Cu–Cu distance is  $d = 3.422$  Å and the interdimer spacing along the chains is  $u = 7.00$  Å. We have grown single crystals with typical masses of 5–10 mg by slow cooling of saturated methanol solutions. Crystals of this size were used for ac susceptibility and specific heat measurements. The zero-field ac susceptibility for  $T > 2$  K was measured in a commercial SQUID magnetometer. The heat capacity was measured in a dilution refrigerator using the relaxation method [22] in magnetic fields up to 9 Tesla.

Inelastic neutron scattering measurements on a powder sample were performed using the QENS time-of-flight spectrometer at the Intense Pulsed Neutron Source (IPNS) of Argonne National Laboratory. The sample consisted of 5.75 g of powder in an annular aluminum sample can with inner diameter 0.3 cm, outer diameter 1.0 cm, and height 12.75 cm. These dimensions were chosen to match the QENS beam size, while keeping the transmission through the hydrogenous sample above 50%.

QENS is an inverse geometry time of flight spectrometer operating at a fixed final energy  $E_f = 3.635$  meV selected by Bragg reflection from three horizontally-focusing pyrolytic graphite PG(002) analyzer systems. The resulting elastic energy resolution is  $\delta E = 0.12$  meV Full Width at Half Maximum (FWHM). Each channel is also equipped with a cooled BeO filter which rejects neutrons with  $E_f > 3.7$  meV through Bragg diffraction. The analyzers can rotate about the sample on a common rotation stage whose angular setting,  $v$  can vary from 0 to 30°. The mean scattering angles,  $2\theta$ , of the three analyzer systems are  $v + 25$ °,  $105 - v$ , and  $v + 115$ ° respectively, and the angular acceptances  $\delta 2\theta$  are 7.5°, 15°, and 15°.

The magnetic neutron scattering cross section of a powder sample at wave vector transfer,  $Q$ , and energy transfer,  $\hbar\omega$  can be written [23]

$$\frac{d^2\sigma}{d\Omega dE'} = \frac{k'}{k} N r_0^2 \left| \frac{g}{2} f(\mathbf{Q}) \right|^2 2\mathcal{S}(Q, \omega) \quad (2)$$

where  $r_0 = 5.38$  fm,  $N$  is the number of copper ions in the sample,  $f(\mathbf{Q})$  is the magnetic form-factor [24], and  $\mathcal{S}(Q, \omega)$  is the spherically averaged scattering function:

$$\mathcal{S}(Q, \omega) = \int \frac{d\Omega_{\hat{Q}}}{4\pi} \frac{1}{2} \sum_{\alpha\beta} (\delta_{\alpha\beta} - \hat{Q}_\alpha \hat{Q}_\beta) \mathcal{S}^{\alpha\beta}(\mathbf{Q}, \omega). \quad (3)$$

The dynamic spin correlation function is given by

$$\mathcal{S}^{\alpha\beta}(\mathbf{Q}, \omega) = \frac{1}{2\pi\hbar} \int dt e^{i\omega t} \frac{1}{N} \sum_{\mathbf{R}\mathbf{R}'} < S_{\mathbf{R}}^\alpha(t) S_{\mathbf{R}'}^\beta(0) > e^{-i\mathbf{Q}\cdot(\mathbf{R}-\mathbf{R}')}. \quad (4)$$

The following corrections were applied to the neutron counts in the time–histograms associated with each of the three analyzer systems. First a time independent background measured for  $\hbar\omega \approx -E_f$  was subtracted. Then the data was scaled to the shifted time–dependent count rate in a pre–sample fission monitor, and finally the data was converted into  $\hbar\omega$ –histograms. This procedure yields  $\hbar\omega$ –dependent data,  $I(Q, \hbar\omega)$ , which is related to the scattering cross section through convolution with a resolution function as follows

$$I(Q, \hbar\omega) = \mathcal{C} \int dQ' \hbar d\omega' \mathcal{R}_{Q\omega}(Q - Q', \omega - \omega') \frac{k}{k'} \frac{d^2\sigma}{d\Omega dE'}(Q', \hbar\omega'), \quad (5)$$

In this expression the resolution function  $\mathcal{R}_{Q\omega}$  is assumed to be normalized to unity:

$$\int dQ' \hbar d\omega' \mathcal{R}_{Q\omega}(Q', \omega') = 1 \quad (6)$$

For a hydrogenous sample such as CuHpCl the elastic intensity is dominated by the incoherent nuclear scattering cross section which reads

$$\frac{d^2\sigma}{r\Omega dE'} = N \sum_{\mathbf{r}} (b_{\mathbf{r}}^i)^2 \delta(\hbar\omega). \quad (7)$$

The summation here is over the nuclei associated with a single copper atom. We used the integrated elastic intensity to determine the spectrometer constant,  $N\mathcal{C}$ :

$$N\mathcal{C} = \frac{\int_{-\epsilon}^{\epsilon} \hbar d\omega I(Q, \hbar\omega)}{\sum_{\mathbf{r}} (b_{\mathbf{r}}^i)^2} \quad (8)$$

With this number we derived a normalized intensity in units suitable for comparison to theories of  $\mathcal{S}(Q, \omega)$ ,

$$\tilde{I}(Q, \hbar\omega) = \frac{I(Q, \hbar\omega)}{r_0^2 N\mathcal{C}} \quad (9)$$

The magnetic contribution to this quantity is related to the spherically averaged dynamic spin correlation function of Eq. (3) as follows:

$$\tilde{I}_m(Q, \hbar\omega) = 2 \int dQ' \hbar d\omega' \mathcal{R}_{Q\omega}(Q - Q', \omega - \omega') \left| \frac{g}{2} f(\mathbf{Q}') \right|^2 \mathcal{S}(Q', \omega') \quad (10)$$

### III. EXPERIMENTAL RESULTS

#### A. Magnetic Susceptibility

Fig. 2 shows the zero-field ac susceptibility of CuHpCl single crystals. The characteristic rounded peak of a 1D AFM appears at  $T_p = 8$  K. Fitting a Curie-Weiss law to high temperature data (30 K  $< T < 200$  K) gives a Curie-Weiss temperature  $\Theta_{CW} = -6.05(1)$  K. Below the peak  $\chi$  drops much more rapidly than for the linear S=1/2 chain with only NN interactions [25], and tends to zero at low temperatures. These data are consistent with previous powder susceptibility measurements [14,15]. The solid lines are a fit based on exact diagonalization of a spin-ladder model which will be discussed in detail below.

#### B. Specific Heat

Figure 3 shows the specific heat  $C(H, T)$  of CuHpCl vs  $T$  in fixed fields up to  $H = 9$  T. No subtraction of the lattice specific heat has been attempted, but as the data are strongly field-dependent and show no sign of a contribution to  $C \propto T^3$  out to  $T = 8$  K, the features we observe are evidently dominated by the spin degrees of freedom. In zero field,  $C$  shows a broad maximum at  $T \approx 4.5$  K, below which it drops rapidly to zero. As the field is increased ( $H = 3$  and 5 T) the maximum in  $C$  broadens and shifts to lower  $T$ , indicating a transfer of spectral weight to lower energies. The qualitative low- $T$  behavior remains the same as for  $H = 0$ , however, as may be seen from the semi-logarithmic plot of  $C$  vs  $1/T$  of the  $H = 0, 3$  and 5 T data shown in Fig. 4. All three data sets approach straight lines in the limit  $1/T \rightarrow \infty$  indicating that  $C(T)$  is exponentially activated. The change in slope with field indicates that the activation energy decreases with increasing  $H$ . This may be quantitatively related to the closure of the spin gap with field, as will be discussed in Sect. IV B below.

As  $H$  is increased further, the shift of spectral weight to lower energy continues as shown in Fig. 3. As the critical field  $H_{c1} \approx 7$  T [14,15] where the gap closes is passed, the curvature of the low- $T$  data changes, and first a shoulder and then a second broad peak appear at  $T \approx 1$  K. Above  $H_{c1}$ , a cusp-like anomaly also becomes visible on top of this second peak. These low- $T$  features are shown in more detail in Fig. 5, where we plot  $C/T$  vs  $T^2$  for  $T < 1.4$  K. The cusp can clearly be seen at  $H = 8$  T and  $H = 9$  T, and below the cusp,  $C(T) \propto T^3$ . These features suggest that above  $H_{c1}$  a phase transition occurs to a field-induced ordered state. A cusp is not as clearly visible at  $H = 7.5$  T, but below the pronounced knee in that data set  $C(T) \propto T^3$ , indicating that at this field the system is also ordered. In contrast, for  $H = 6.6$  T, at the lowest temperatures shown  $C$  drops faster than  $T^3$ , suggesting the existence of a small gap [26]. The inset to Fig. 5 shows the  $H$ - $T$  phase diagram of CuHpCl as determined from these data in combination with our earlier field-dependent susceptibility measurements [14], and the magnetization data of Chaboussant *et al.* [15]. We note that this phase diagram, and indeed the overall features of the susceptibility and field-dependent specific heat are quite similar to other gapped spin chains, such as the alternating chain Cu(NO<sub>3</sub>)<sub>2</sub> · 2.5H<sub>2</sub>O [2].

### C. Neutron Scattering

Figure 6 shows the normalized angular average  $\tilde{I}(\hbar\omega)$  of neutron scattering from CuHpCl. The normalization of  $\tilde{I}(\hbar\omega)$  is as described in Eq. 9, and the angular average was carried out over the full accessible range of scattering angle  $21^\circ < 2\theta < 153^\circ$ . The intense elastic peak arises from incoherent nuclear scattering as discussed in Sect. II and the inelastic scattering for  $\hbar\omega > 2$  meV comes from incoherent inelastic nuclear scattering. There is however also a broad peak for  $0.8$  meV  $< \hbar\omega < 1.4$  meV which we now show is associated with magnetic scattering. To isolate this feature we measured the incoherent nuclear scattering from 5.4 g of the non-magnetic organic compound benzophenone (dibenzyl ketone). The material and the amount were chosen to match the total elastic cross section of CuHpCl, and filled approximately the same volume as the CuHpCl sample. 33 mg of boron carbide was added to the benzophenone to match the absorption cross-section of CuHpCl. The resulting integrated elastic intensity from the benzophenone sample was only 15% stronger than for CuHpCl. We applied a scale factor to the benzophenone data so that its integrated elastic intensity matched that of  $\tilde{I}(Q, \hbar\omega)$  for CuHpCl. The angular-averaged data for benzophenone are shown as open squares in Fig. 6. As may be seen, the line shapes of the elastic peaks are indistinguishable, which allows us to use the benzophenone data to approximately subtract the non-magnetic contributions to the neutron scattering intensity from CuHpCl. A small constant term of 0.03 meV per Cu was added to ensure that the difference data for  $\hbar\omega << -k_B T$  averages to zero as required by detailed balance.

The resulting difference data,  $\tilde{I}_m(\hbar\omega)$ , is shown in Fig. 7(a). The only feature in these data above background is the peak centered at  $\hbar\omega = 1.15$  meV. To determine whether this feature is magnetic or is due to phonons, we measured the scattering from the CuHpCl sample at  $T = 20$  K and subjected those data to the same background corrections as the low temperature data. The result is shown in Fig. 7 (b). The peak broadens and a mirror image of it emerges for  $\hbar\omega < 0$  as expected from detailed balance [23]. This behavior establishes that the difference data shown in Fig. 7(a) is indeed magnetic and is a measure of the the angular averaged magnetic scattering intensity for CuHpCl:

$$\tilde{I}_m(\hbar\omega) = \int_{21^\circ}^{153^\circ} d2\theta \tilde{I}_m(Q, \hbar\omega), \quad (11)$$

which may related to  $\mathcal{S}(Q, \omega)$  through Eq. 10. The data shows that magnetic scattering occurs only above a gap,  $\Delta \approx 0.8$  meV and that the bandwidth for the magnetic excitation spectrum is 0.7 meV.

Having established the magnetic “density of states,” we turn to the wave vector dependence of the magnetic scattering cross section which contains information about spatial spin correlations. In Fig. 8 we show the  $Q$ -dependence of the magnetic scattering integrated over the range of energies with appreciable magnetic signal:

$$\tilde{I}_m(Q) = \int_{0.8 \text{ meV}}^{1.5 \text{ meV}} \hbar d\omega \tilde{I}_m(Q, \hbar\omega), \quad (12)$$

The limited sampling density and statistics do not allow us to clearly discern any features in the data. We note only that as expected for magnetic scattering and not for inelastic scattering from phonons the intensity decreases with increasing wave vector transfer. The lines through the data in Figs. 7 and 8 result from a model calculation to be discussed below.

## IV. DISCUSSION

### A. Analysis of susceptibility data

In their pioneering work on CuHpCl [13], Chiari *et al.* suggested that this material may realize the Hamiltonian  $\mathcal{H}$  of Eq. (1). On the basis of high temperature susceptibility data alone, they were not able to place strong constraints on the possible models, although they concluded that the intra-dimer and inter-dimer NN interactions  $J_1$  and  $J_3$  are different as indicated in Fig. 1.

We have previously analyzed some of the data on this material in terms of the isolated dimer model ( Eq. (1) with  $J_3 = 0, J_2 = 0$ ), the alternating near-neighbor model ( $J_2 = 0, J_3/J_1 \in [0, 1]$ ), and the next-nearest-neighbor model without alternation ( $J_3/J_1 = 1, J_2/J_1 \in [0.3, 0.7]$ ). None of these provided a satisfactory fit to our powder susceptibility data [14]. Chaboussant *et al.* analyzed their powder susceptibility data in terms of both the alternating chain and the spin ladder ( $J_3 = 0$ ) models, using high temperature series expansions [15]. While both models fit the data, from structural considerations they concluded that the ladder is more likely. A comparison of their magnetization

data to exact diagonalization calculations for the ladder model [27] found good agreement for  $J_2/J_1 = 0.18$ , although additional improvement to the fit was found if a small ferromagnetic diagonal coupling  $J_3$  was added.

To analyze our single crystal susceptibility data, we carried out a systematic search of the parameter space of the Hamiltonian in Eq. (1). We diagonalized chains up to length  $N = 14$  for values of the exchange constants on a large grid in  $J_2/J_1 - J_3/J_1$  space. The calculated eigenvalues for each point were used to generate  $\chi(T/J_1, H = 0)$  on the interval  $T/J_1 \in [0.2, 20]$ . Below  $T/J_1 = 0.2$ , the results for  $N = 12$  deviated from those for  $N = 14$  by greater than 1%, due to effects of the finite system size. By tri-linearly interpolating in this 3D mesh of  $(T/J_1, J_2, J_3)$ , we could generate  $\chi(T)$  for arbitrary  $J_1, J_2$ , and  $J_3$ . The accuracy of this procedure was checked by comparing the interpolated  $\chi(T)$  between mesh points against exact diagonalization at those same values. The difference was found to be less than 1 part per thousand. The parameter space was constrained by the measured upper critical field  $H_{c2} = 13.3$ T, or 18.8K [15], which occurs at  $g\mu_B H_{c2} = \max(J_1 + J_3, J_1 + 2 * J_2)$  where the energy of the spinwaves from the ferromagnetic state change sign.

A simultaneous fit to both the a-axis and b-axis data in Fig. 2 gave  $g_a = 2.15(1)$ ,  $g_b = 2.04(1)$ ,  $J_1/k_B = 13.26(4)$  K,  $J_2/k_B = 2.4(3)$  K, and  $J_3/k_B = 1.1(6)$  K. The error bars quoted correspond to the intervals over which the reduced  $\chi^2$  deviates by less than  $1/N_{free}$  from its minimum value. Here  $N_{free}$  is the number of data points minus the number of parameters in the fit. The results are shown as solid curves in the figure. The values of the g-factors in our fits are consistent with the values determined by EPR, [15] and the values for  $J_1$  and  $J_2$  are in good agreement with the analysis of the magnetization data, although  $J_3$  on which our error bars are large differs in sign.

The fit indicates that the intra rung coupling  $J_1$  exceeds the inter-rung coupling  $J_2$  by a factor of approximately five. In this strong-coupling limit the zeroth order approximation to the ground state is simply a chain of non-interacting rung singlets and the excited states are localized triplets at energy  $\hbar\omega = J_1$ . Clearly this approximation is too coarse since it cannot account for the finite bandwidth of the magnetic excitation spectrum which is evident in the neutron scattering data (Fig. 7 (a)). We therefore must take the inter-rung coupling into account, and the most straightforward way to do this is through a perturbation expansion. Neglecting effects of  $J_3$ , the excited states then become propagating triplets with a dispersion relation [28]

$$\begin{aligned} \hbar\omega(\tilde{q}) = J_1 &[1 + \frac{J_2}{J_1} \cos \tilde{q} + \frac{1}{4}(\frac{J_2}{J_1})^2(3 - \cos 2\tilde{q}) \\ &- \frac{1}{8}(\frac{J_2}{J_1})^3(2 \cos \tilde{q} + 2 \cos 2\tilde{q} - \cos 3\tilde{q} - 3) + O(\frac{J_1}{J_2})^4], \end{aligned} \quad (13)$$

where  $\tilde{q} = \mathbf{Q} \cdot \mathbf{u}$  is the component of wavevector transfer along the chain. For our ladder model the higher order terms in Eq. (13) are very small. For example  $J_1(J_2/J_1)^2 = 0.039$  meV which could be compared to the energy resolution of our neutron scattering experiment which is  $\delta E = 0.12$  meV FWHM. Therefore we approximate the dispersion relation with

$$\hbar\omega(\mathbf{Q}) = J_1 + J_2 \cos(\mathbf{Q} \cdot \mathbf{u}). \quad (14)$$

The corresponding gap in the magnetic excitation spectrum is

$$\Delta = J_1 - J_2 \quad (15)$$

## B. Analysis of Specific Heat Data

To test the spin ladder model we compare its predictions to the low temperature specific heat data. If we approximate the dispersion relation by Eq. (14) and neglect interactions between propagating triplet excitations, the zero-field specific heat in the low temperature limit takes the form

$$C = \frac{nR}{2\sqrt{2\pi}} \left( \frac{\Delta}{k_B T} \right)^{3/2} \sqrt{\frac{\Delta}{J_2}} \exp(-\Delta/k_B T), \quad (16)$$

measured in  $J/(K \text{ mol-Cu})$  with  $n = 3$  being the number of low energy modes in a Brillouin zone. The solid line through the zero-field data in Fig. 4 is a fit to this functional form. It yields  $\Delta = 0.89(1)$  meV, which is close to the value  $\Delta = J_1 - J_2 = 0.93(3)$  meV predicted by the spin ladder model. If we assume that the main effect of fields  $H < H_{c1}$  on the spectrum is to Zeeman-split the triplet mode, then Eq. 16 should remain a good description of the

low- $T$  behavior of  $C(H, T)$ , although both  $n$  and  $\Delta$  may now vary with field. The fits shown in Fig. 4 for  $H = 3$  T and 5 T yield  $\Delta = 0.55(4)$  meV and  $n = 1.3(3)$ , and  $\Delta = 0.24(4)$  and  $n = 0.6(2)$ , respectively. This reduction of  $n$  with field is qualitatively consistent with spin-splitting of the triplet, as the lowest-energy band should dominate the specific heat in the range  $k_B T < \Delta(H)/4$  where these fits were done. The gap vs field determined from the fits is shown in the inset of Fig. 4 together with the estimated value of the gap at  $H = 6.6$  T [26]. The observed reduction of  $\Delta$  with  $H$  is consistent with the linear behavior expected for the Zeeman-splitting of the triplet. The data in the inset are fit by the line shown, which has a slope of  $-2.09(1)\mu_B$ , and extrapolates to  $\Delta = 0$  at  $H = 7.2(1)$  T, in accord with  $H_{c1}$  determined by other methods [14,15].

### C. Single mode approximation to $\mathcal{S}(Q, \omega)$

A spin ladder Hamiltonian with  $J_3 \approx 0$  thus can account for the temperature dependent susceptibility and the low temperature specific heat of CuHpCl. We now discuss to what extent the spin ladder model can account for our neutron scattering data.

Exact diagonalization studies suggest that most of the spectral weight for magnetic excitations is associated with the resonant triplet mode [29]. Therefore we use the single mode approximation: that the dynamic spin correlation function takes the form

$$\mathcal{S}^{\alpha\beta}(\mathbf{Q}, \hbar\omega) = \mathcal{S}(\mathbf{Q})\delta(\hbar\omega - \hbar\omega(\mathbf{Q}))\delta_{\alpha\beta}, \quad (17)$$

Two sum-rules [30] place further constraints on  $\mathcal{S}(\mathbf{Q}, \omega)$ :

$$\int d^3\mathbf{Q} \int \hbar d\omega \sum_{\alpha} \mathcal{S}^{\alpha\alpha}(\mathbf{Q}, \omega) / \int d^3\mathbf{Q} = S(S+1) \quad (18)$$

$$\hbar^2 \int \omega d\omega \mathcal{S}^{\alpha\beta}(\mathbf{Q}, \omega) = < [\mathcal{H}, S_{\mathbf{Q}}^{\alpha}], S_{-\mathbf{Q}}^{\beta} >, \quad (19)$$

Where

$$S_{\mathbf{Q}}^{\alpha} = \frac{1}{N} \sum_{\mathbf{R}} S_{\mathbf{R}}^{\alpha} e^{-i\mathbf{Q}\cdot\mathbf{R}}. \quad (20)$$

From Eqs. (19), (17), and (1) with  $J_3 = 0$  it can be shown that

$$\mathcal{S}(\mathbf{Q}) = -\frac{2}{3} \frac{1}{\hbar\omega(\mathbf{Q})} \left[ J_1 \langle \mathbf{S}_{2i} \cdot \mathbf{S}_{2i+1} \rangle (1 - \cos(\mathbf{Q} \cdot \mathbf{d})) + J_2 (\langle \mathbf{S}_{2i} \cdot \mathbf{S}_{2i+2} \rangle + \langle \mathbf{S}_{2i-1} \cdot \mathbf{S}_{2i+1} \rangle) (1 - \cos(\mathbf{Q} \cdot \mathbf{u})) \right] \quad (21)$$

Here  $\mathbf{d}$  and  $\mathbf{u}$  are vectors connecting spins within a rung and along an arm of the ladder, respectively, and  $\langle \mathbf{S}_i \cdot \mathbf{S}_j \rangle$  are the corresponding groundstate equal time correlation functions. Because we are interested in the strong rung coupling limit we neglect interdimer correlations and adopt a simplified version of Eq. (21)

$$\mathcal{S}(\mathbf{Q}) \approx -\frac{2}{3} \frac{J_1}{\hbar\omega(\mathbf{Q} \cdot \mathbf{u})} \langle \mathbf{S}_{2i} \cdot \mathbf{S}_{2i+1} \rangle (1 - \cos(\mathbf{Q} \cdot \mathbf{d})). \quad (22)$$

In this approximation the coupling along the ladder is reflected only in the one-dimensional dispersion relation  $\hbar\omega(\mathbf{Q} \cdot \mathbf{u})$  of Eq. (14). Requiring that  $\mathcal{S}(\mathbf{Q}, \omega)$  defined in this way satisfies the total moment sum rule of Eq. (18) fixes

$$\langle \mathbf{S}_{2i} \cdot \mathbf{S}_{2i+1} \rangle = -S(S+1)(1 - (J_2/J_1)^2)^{1/2}. \quad (23)$$

With the exchange constants determined from the susceptibility measurements, this gives a model that may be compared to the data of Figs. 7 and 8 with no adjustable parameters.

After inserting Eq. (22) in Eq. (3), the spherical average may be computed exactly, yielding

$$\begin{aligned} \mathcal{S}(Q, \hbar\omega) = & -\frac{2J_1 \langle \mathbf{S}_{2i} \cdot \mathbf{S}_{2i+1} \rangle}{3Qu} \sum_{Q_i \leq Q} \frac{1 - J_0(d \sin \alpha \sqrt{Q^2 - Q_i^2}) \cos(Q_i d \cos \alpha)}{\hbar\omega \sqrt{(J_1 + J_2 - \hbar\omega)(\hbar\omega - (J_1 - J_2))}} \\ & \times \Theta(J_1 + J_2 - \hbar\omega) \Theta(\hbar\omega - (J_1 - J_2)) \end{aligned} \quad (24)$$

where  $J_0(x)$  is a Bessel function,  $\alpha = 55.4^\circ$  is the angle between  $\mathbf{u}$  and  $\mathbf{d}$ , [13] and the  $Q_i = (1/u) \cos^{-1}[(\hbar\omega - J_1)/J_2]$  are the solutions of Eq. (14) at fixed  $\hbar\omega$ . Convolution of Eq. (24) with the instrumental resolution and summing over the values of  $2\theta$  used in the experiment gives the solid curve in Fig. 7(a). Several features of this curve are worth noting. First, the mean energy and bandwidth match the data quite well. This is to be expected since the model after all was chosen to account for susceptibility data whose temperature dependence controlled by these two features of the magnetic excitation spectrum. Second the area under the data closely matches the area under the calculated curve. This indicates that the inelastic peak which we have detected contains most of the magnetic neutron scattering to be expected from the copper ions in CuHpCl.

The model does not, however, reproduce the shape of the data very well. The two peaks in the model correspond to singularities in the one-dimensional magnetic density of states at  $\hbar\omega = J_1 \pm J_2$ . The data does not show these peaks, being instead peaked near the center of the band. Note that inclusion of the interdimer correlations from Eq. 21, which were neglected in our approximate treatment (Eq. 22), will only make the agreement of model with data worse, as that produces a contribution to  $S(Q, \omega)$  with a single peak at  $\hbar\omega = J_1 - J_2$ . We also note that the data show an unexpected tail of scattering intensity below the lower bound predicted by the model. This is consistent with specific heat data [14] that show a gap  $\Delta = 0.89(1)$  meV, which is close to the gap seen from neutron scattering data but less than the gap  $\Delta = J_1 - J_2 = 0.93(3)$  meV predicted by the ladder model derived from the susceptibility data.

Fig. 8 compares the data and the model calculation of the  $Q$ -dependent energy integrated intensity (Eq. 12). For CuHpCl, this is the first comparison of data which is sensitive to the geometry of the spin system to predictions of the ladder model. The data bear no evidence of the maximum in  $\tilde{I}(Q)$  predicted by the spin ladder model for  $Q \approx 1.3\text{\AA}^{-1}$ , which raises the question of whether the ladder model is the correct description of CuHpCl.

## V. CONCLUSION

We have reported experiments on CuHpCl which establish that this system has a gap in its magnetic excitation spectrum and which determine the magnetic bandwidth. Our susceptibility and specific heat data can be accounted for in terms of a spin-ladder model with intra-rung coupling  $J_1 = 1.143(3)$  meV and two mutually frustrating inter-rung interactions:  $J_2 = 0.21(3)$  meV and  $J_3 = 0.09(5)$  meV. Not surprisingly this model reproduces the gross features of the magnetic density of states as probed by neutron scattering. However our neutron scattering data do not show the Van-Hove singularities and the  $Q$ -dependence predicted by a single mode approximation of the excitation spectrum in a simple spin ladder model. It is possible that a refined calculation of  $S(Q, \omega)$  for a spin ladder would resolve these discrepancies, but it is clear that further experiments, particularly neutron scattering on deuterated single crystals, are required to definitively establish the spin Hamiltonian for CuHpCl.

## ACKNOWLEDGMENTS

This work was supported by the NSF under grants DMR-9357518 and DMR-9302065, the DOE BES-Materials Science contract W-31-109-ENG-38 with IPNS-ANL, and by the David and Lucile Packard Foundation.

---

- [1] J. C. Bonner, H. W. Blöte, J. W. Bray, I. S. Jacobs, *J. Appl. Phys.* **50**, 1810 (1979)
- [2] J. C. Bonner, S. A. Friedberg, H. Kobayashi, D. L. Meier, and H. W. J. Blöte, *Phys. Rev. B* **27**, 248 (1983).
- [3] B. S. Shastry and B. Sutherland, *Phys. Rev. Lett.* **47**, 964 (1981).
- [4] C. K. Majumdar and D. K. Ghosh, *J. Phys. C* **3**, 911 (1969).
- [5] S. R. White and I. Affleck, *Phys. Rev. B* **54**, 9862 (1996).
- [6] E. Dagotto and T. M. Rice, *Science* **271**, 618 (1996).
- [7] S. Gopalan, T. M. Rice, and M. Sigrist, *Phys. Rev. B* **49**, 8901 (1994); S. R. White, R. M. Noack, and D. J.

Scalapino, Phys. Rev. Lett. **73**, 886 (1994); S. P. Strong and A. J. Millis, Phys. Rev. Lett. **69**, 2419 (1992); M. Azzouz, L. Chen, and S. Moukouri, Phys. Rev. B **50**, 6233 (1994).

[8] J. Eckert, D. E. Cox, G. Shirane, S. A. Friedberg, and H. Kobayashi, Phys. Rev. B **20**, 4596 (1979).

[9] M. Arai, M. Fujita, M. Motokawa, J. Akimitsu, and S. M. Bennington, Phys. Rev. Lett. **77**, 3649 (1996).

[10] M. Ain, J. E. Lorenzo, L. P. Regnault, G. Dhaleine, A. Revcolevschi, B. Hennion, and T. Jolicoeur, Phys. Rev. Lett. **78**, 1560 (1997).

[11] M. Azuma, Z. Hiroi, M. Takano, K. Ishida, and Y. Kitakoka, Phys. Rev. Lett. **73**, 3643 (1994).

[12] S. A. Carter, B. Batlogg, R. J. Cava, J. J. Krajewski, W. F. Peck, Jr., and T. M. Rice, Phys. Rev. Lett. **77**, 1378 (1996).

[13] B. Chiari, O. Piovesana, T. Tarantelli, and P. F. Zanazzi, Inorg. Chem. **29**, 1172 (1990).

[14] P. R. Hammar and D. H. Reich, J. App. Phys. **79**, 5392 (1996)

[15] G. Chaboussant, P. Crowell, L. P. Lévy, O. Poivesana, A. Madouri, D. Mailly, Phys. Rev. B **55**, 3046 (1997).

[16] G. Chaboussant, M.-H. Julien, Y. Fagot-Revurat, L. P. Levy, C. Berthier, M. Horvatic, and O. Piovesana, Preprint cond-mat/9706138 (1997).

[17] D. C. Johnston, J. W. Johnson, D. P. Goshorn, and A. J. Jacobson, Phys. Rev. B **35**, 219 (1987).

[18] R. S. Eccleston, T. Barnes, J. Brody, and J. W. Johnson, Phys. Rev. Lett. **73**, 2626 (1994).

[19] A. W. Garrett, S. E. Nagler, T. Barnes, and B. C. Sales, Phys. Rev. B **55**, 3631 (1997).

[20] A. W. Garrett, S. E. Nagler, D. A. Tennant, B. C. Sales, and T. Barnes, Phys. Rev. Lett. **79**, 745 (1997).

[21] R. Chitra, and T. Giamarchi, Phys. Rev. B **55**, 5816 (1997).

[22] R. Bachmann, *et al.*, Rev. Sci. Inst. **42**, 205 (1972).

[23] We use the notation of S.W. Lovesey, *Theory of Neutron Scattering from Condensed Matter*, Clarendon Press, Oxford (1984).

[24] A. J. Freeman and R. E. Watson, Acta. Cryst. **14**, 231 (1961); P. J. Brown, in *International Tables for Crystallography*, A. J. C. Wilson Ed. , Vol. C, Kluwer Academic Publishers, London (1995).

[25] J. C. Bonner and M. E. Fisher, Phys. Rev. **135**, A640 (1964).

[26] We estimate the gap  $\Delta(H = 6.6 \text{ T}) \approx 0.10(5) \text{ meV}$  based on experience with field-induced gaps in other nearly-critical spin chain systems (Dender *et al.*, Phys. Rev. Lett, to appear) that shows the “knee” in a plot of  $C/T$  to reliably occur at  $\approx \Delta/4$ .

[27] C. A. Hayward, D. Poilblanc, and L. P. Lévy, Phys. Rev. B **54**, R12649 (1996)

[28] M. Reigrotzki, H. Tsunetsugu, and T. M. Rice, J. Phys. Condens. Matter **6**, 9235 (1994).

[29] T. Barnes, E. Dagotto, J. Riera, and E. S. Swanson, Phys. Rev. B **47**, 3196 (1993);

[30] P. C. Hohenberg and W. F. Brinkman, Phys. Rev. B **10**, 128 (1974).

FIG. 1. Schematic of chain structure of CuHpCl, indicating possible near-neighbor bond alternation ( $\delta$ ) and next-near-neighbor bonds. The ellipses show how the dimer units stack.

FIG. 2. AC susceptibility  $\chi(T)$  of single crystal CuHpCl with the field oriented along the **a** and **b** axes. The curves differ by a scale factor consistent with the g-factor anisotropy. [15] The solid lines are a fit to exact diagonalizations of the  $J_1$ - $J_2$ - $J_3$  model.

FIG. 3. Magnetic specific heat  $C(H, T)$  vs  $T$  for CuHpCl. At low fields  $C$  is suppressed at low temperatures because of the gap to magnetic excitations. Above  $H_{c1} \approx 7$  T, there is evidence for a phase transition to an ordered state.

FIG. 4. Semi-logarithmic plot of  $C(H, T)$  vs  $1/T$  in the gapped phase showing activated behavior with fits to a spin-ladder model as described in the text. Inset: gap  $\Delta$  determined from fits plus an estimate of gap for  $H = 6.6$  T [26].

FIG. 5.  $C/T$  vs  $T^2$  at low temperatures, showing  $C \propto T^3$  below the temperature of the ordering anomaly at high fields. Inset: putative phase diagram for CuHpCl based on specific heat and magnetization data [14,15], indicating boundary between one-dimensional (1D) disordered and ordered (AF) phases.

FIG. 6. Normalized, angular-averaged inelastic neutron scattering intensity for CuHpCl at  $T = 1.5$  K (solid circles). The full incoherent elastic peak (small circles) is shown reduced in magnitude 1000 times. Also shown is scattering intensity for benzophenone (open squares), used to measure the non-magnetic background for  $-1.5 \text{ meV} \leq \hbar\omega \leq 2 \text{ meV}$ .

FIG. 7. Magnetic, angular-averaged inelastic neutron scattering intensity for CuHpCl obtained after subtracting non-magnetic background in Fig. 6. The reduction of the peak in (a) with increasing  $T$  identifies it as due to spin fluctuations. The solid line in (a) is the predicted intensity based on the spin ladder model derived from susceptibility measurements with no adjustable parameters.

FIG. 8. Wavevector dependence of the energy-integrated magnetic scattering for CuHpCl at  $T = 1.5$  K. Solid line is the prediction of the spin ladder model.

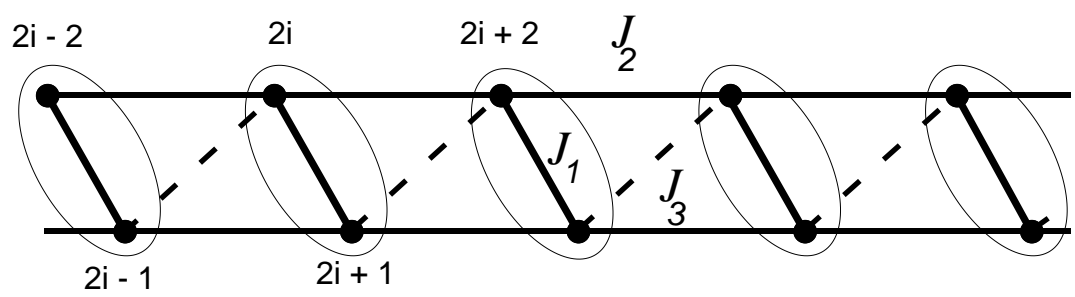


FIG. 1. Hammar , et al.

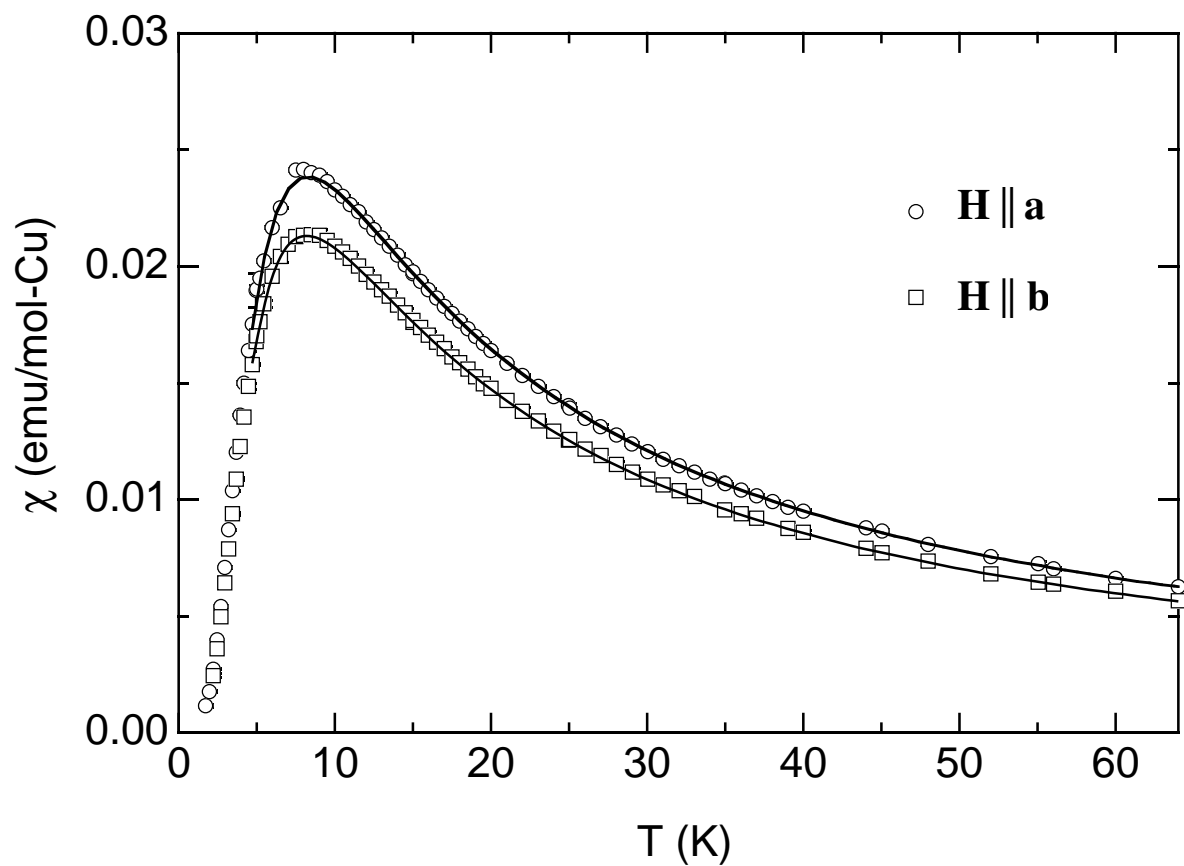


Fig. 2. Hammar, et al.

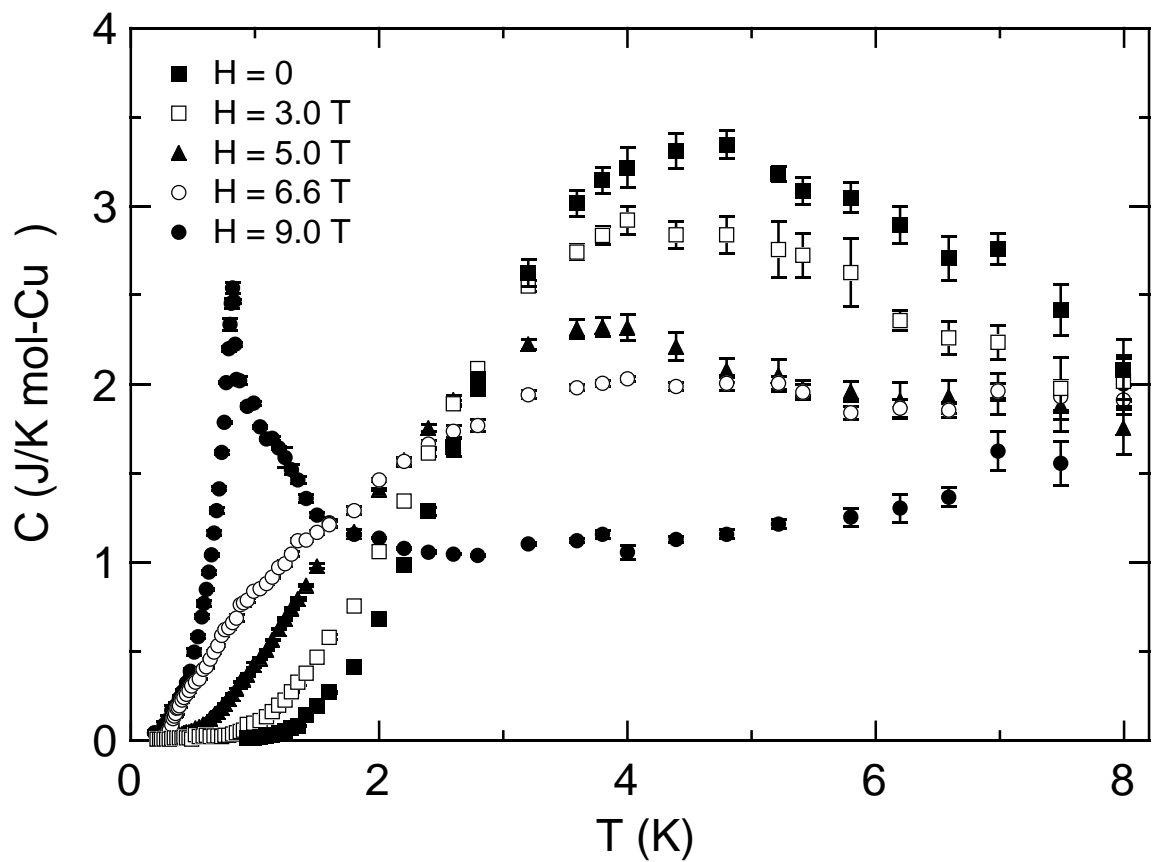


Figure 3: Hammar et al.

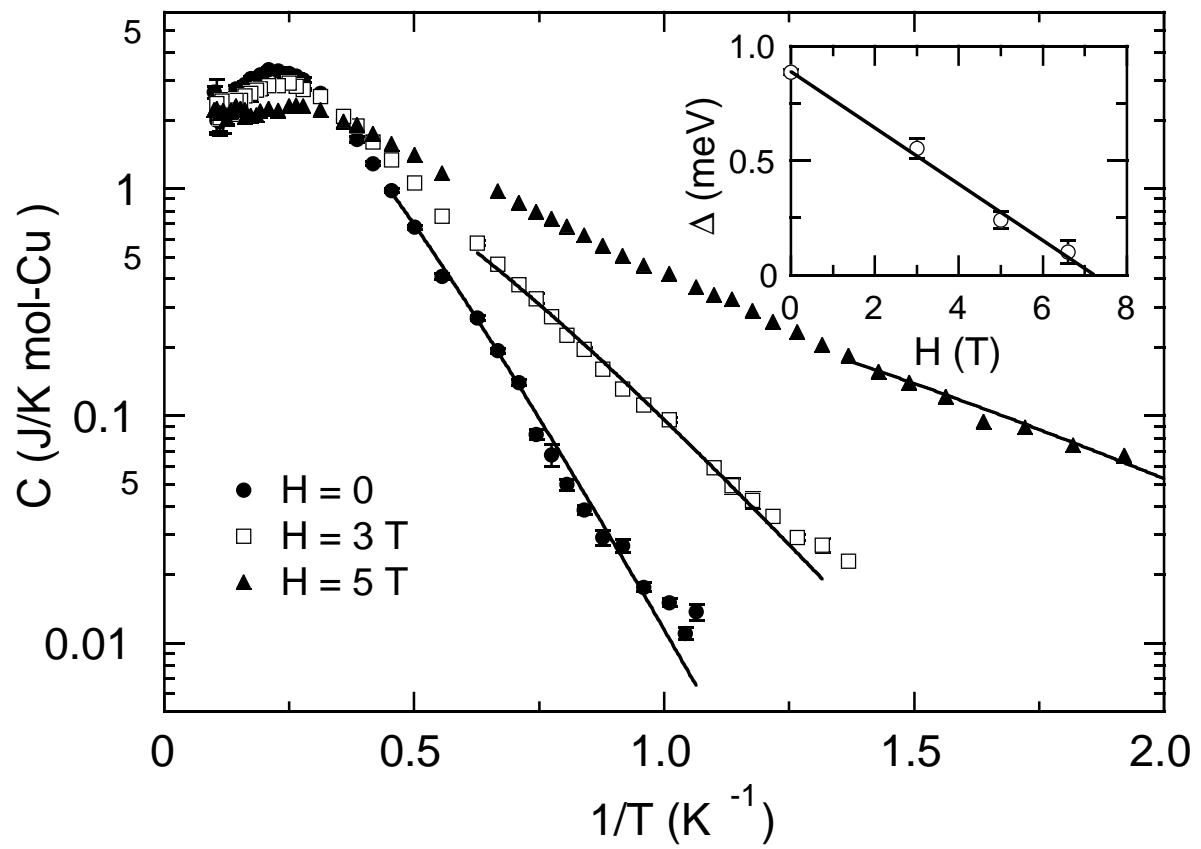


Fig. 4. Hammar, et al.

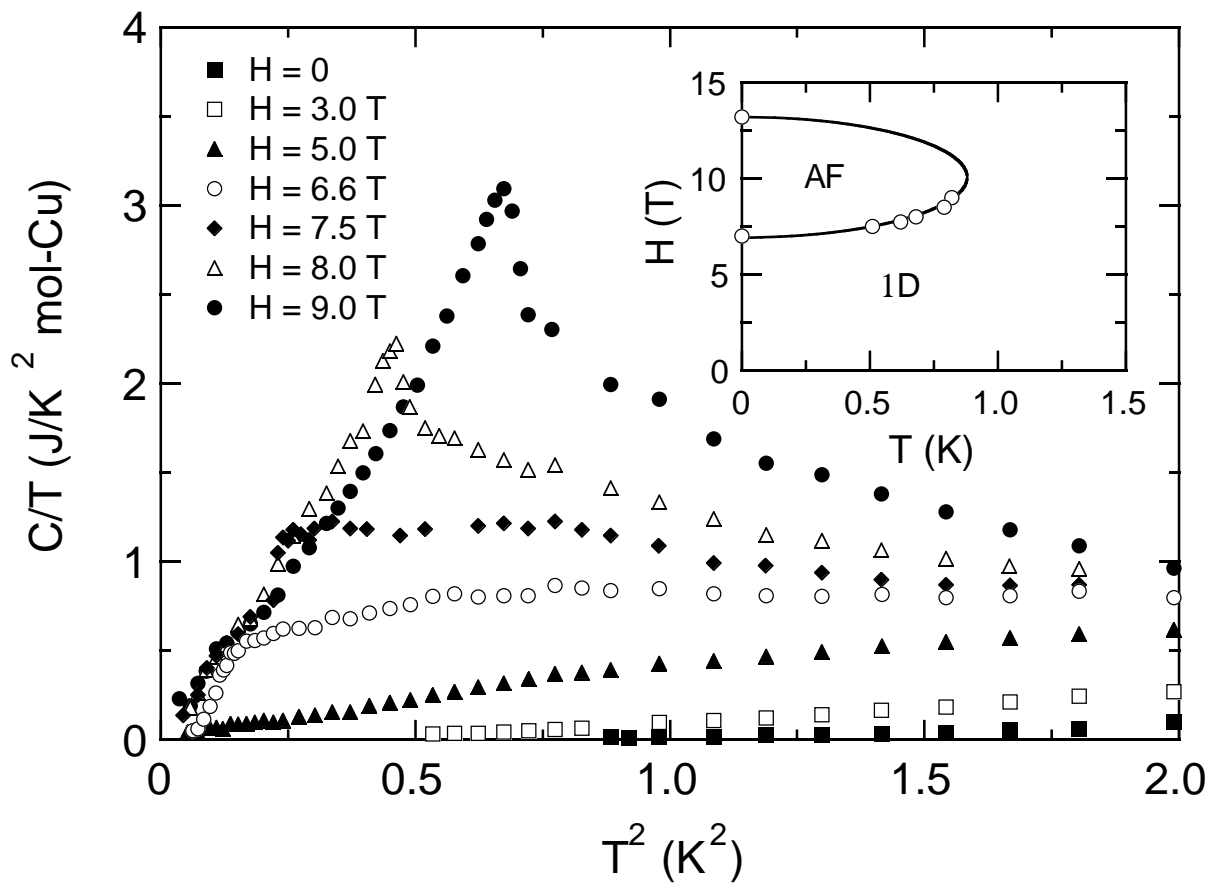


Fig. 5. Hammar, et al.

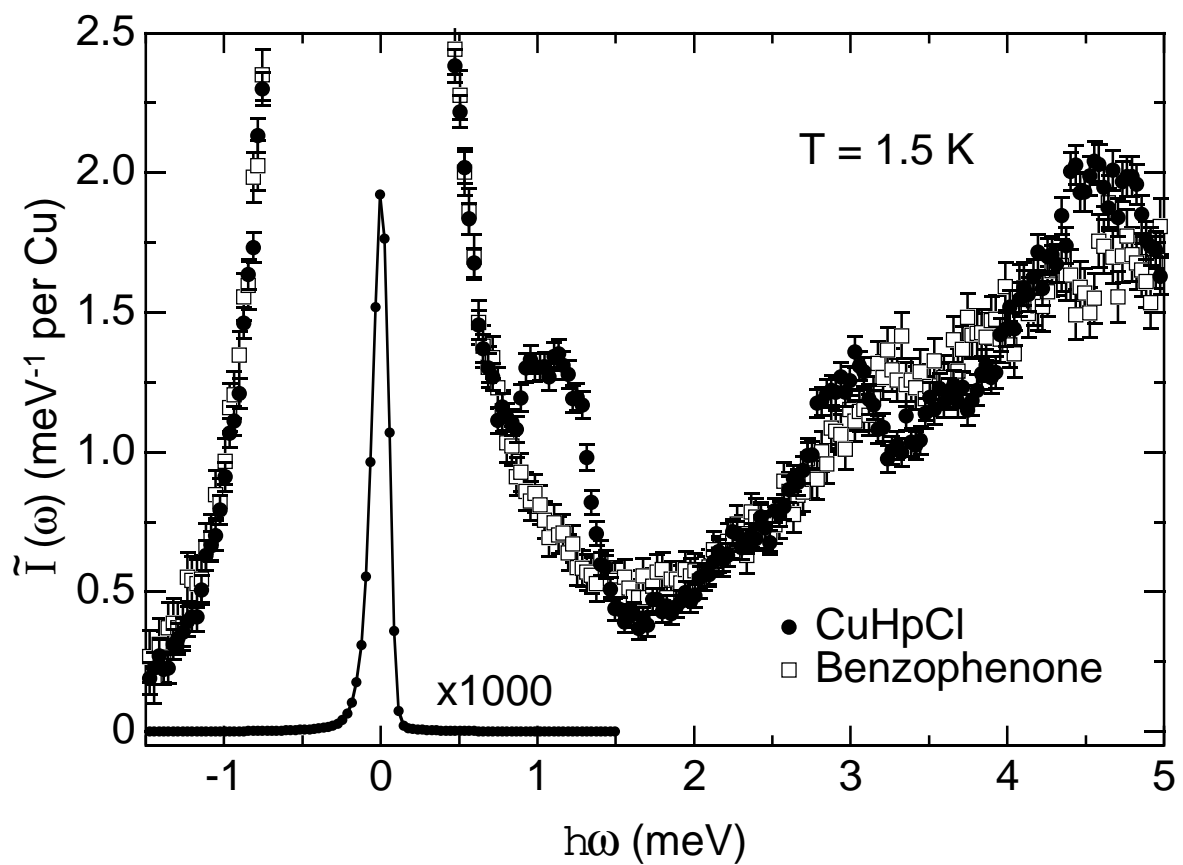


Fig. 6 Hammar, et al.

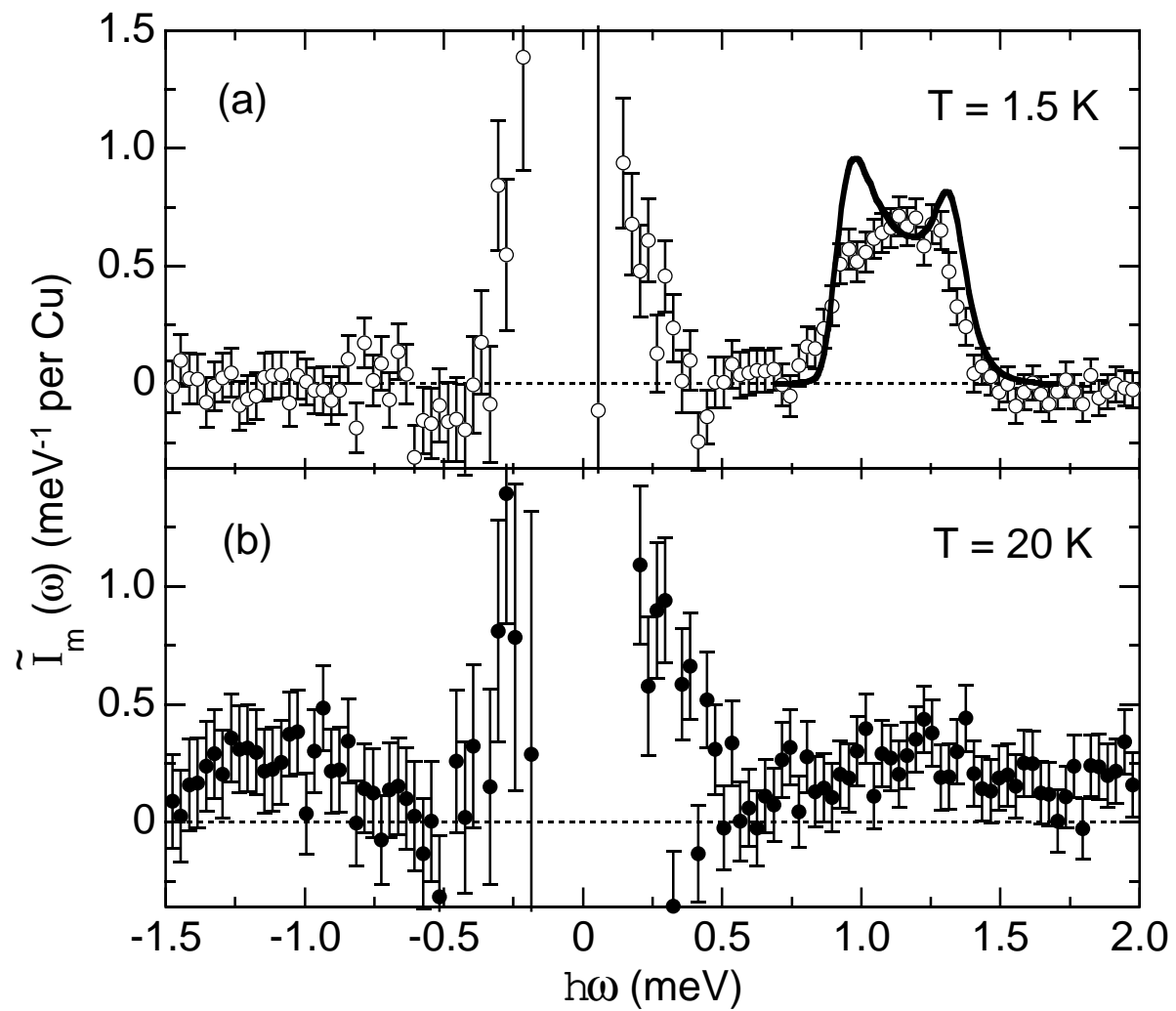


Fig. 7 Hammar, et al.

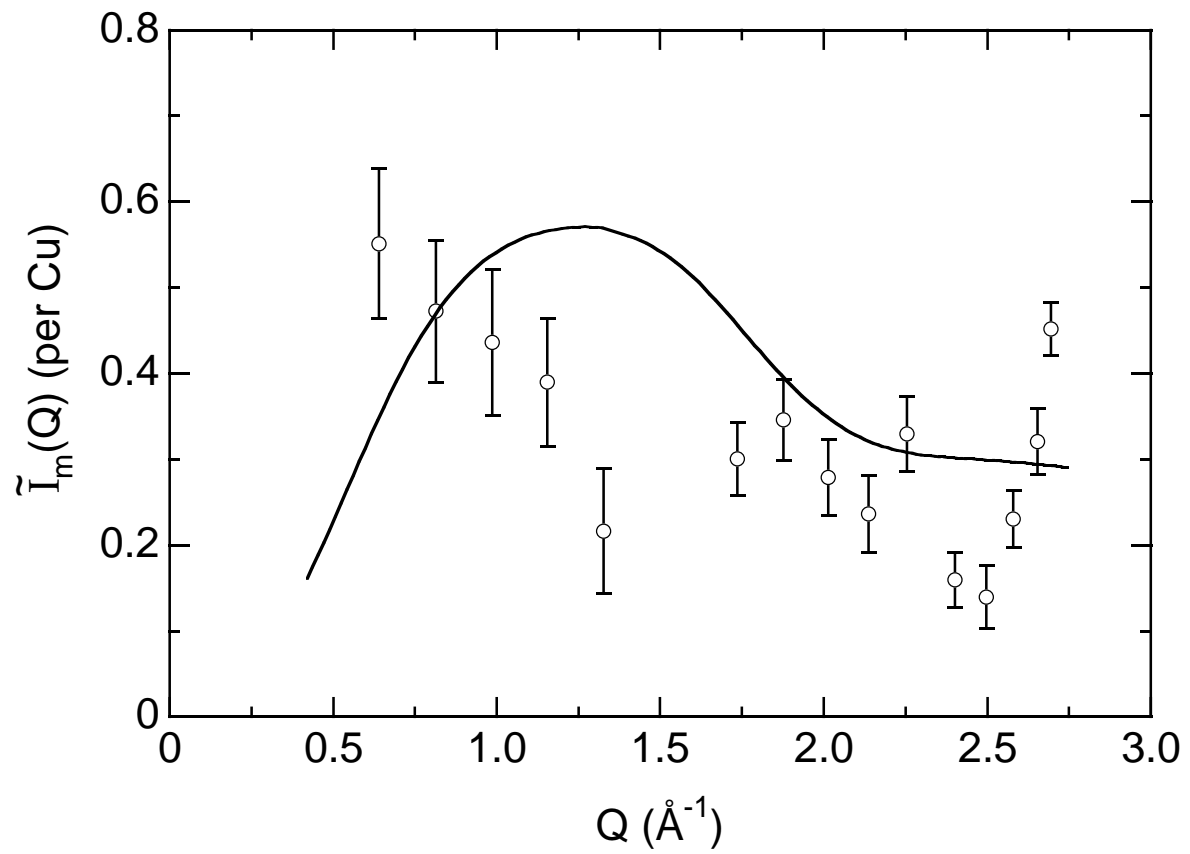


Fig. 8. Hammar, et al.